

Transcriptomic and morphologic vascular aberrations underlying FCDIIb etiology

Received: 31 July 2023

Accepted: 25 March 2025

Published online: 08 April 2025

 Check for updates

Chuantao Fang^{1,2,3,11}, Xiaodan Zhang^{2,11}, Lin Yang^{2,11}, Licheng Sun^{1,11}, Yujia Lu^{1,11}, Yi Liu⁴, Jingjing Guo¹, Min Wang², Yanfeng Tan², Jinsen Zhang², Xin Gao⁵, Li Zhu⁶, Guoping Liu², Maozhi Ren⁷, Jianbo Xiao⁴, Fayong Zhang², Shaojie Ma⁸, Rui Zhao^{2,9,10} ✉, Xinyu Mei¹ ✉ & Dashi Qi^{1,2} ✉

Focal cortical dysplasia type II (FCDII) is a major cause of drug-resistant epilepsy, but genetic factors explain only some cases, suggesting other mechanisms. In this study, we conduct a molecular analysis of brain lesions and adjacent areas in FCDIIb patients. By analyzing over 217,506 single-nucleus transcriptional profiles from 15 individuals, we find significant changes in smooth muscle cells (SMCs) and astrocytes. We identify abnormal vascular malformations and a unique type of SMC that we call “Firework cells”, which migrate from blood vessels into the brain parenchyma and associate with VIM⁺ cells. These abnormalities create localized ischemic-hypoxic (I/H) micro-environments, as confirmed by clinical data, further impairing astrocyte function, activating the HIF-1 α /mTOR/S6 pathway, and causing neuronal loss. Using zebrafish models, we demonstrate that vascular abnormalities resulting in I/H environments promote seizures. Our results highlight vascular malformations as a factor in FCDIIb pathogenesis, suggesting potential therapeutic avenues.

Focal cortical dysplasia (FCD) represents the congenital malformations of the cerebral neocortex, recognized as the most commonly resected epileptogenic lesions in children and the third most common in adults¹. FCD encompasses a wide spectrum of cortical development malformations and is the leading cause of drug-resistant focal epilepsy requiring surgical intervention². These lesions exhibit diverse histopathological abnormalities, complicating their diagnosis and treatment³. According to the International

League Against Epilepsy, FCD is classified into three main types: FCDI involves isolated cortical layering abnormalities; FCDII includes abnormalities in cortical architecture with cytomegalic dysmorphic neurons (CDNs) and balloon cells (BCs); and FCDIII features cortical layering abnormalities associated with other lesions^{4–6}. Among these, FCDII is the most prevalent subtype, characterized by disrupted cortical organization and abnormal neuronal development⁷. It is further divided into FCDIIa, which presents with dysmorphic neurons

¹Center for Clinical Research and Translational Medicine, Yangpu Hospital, School of Medicine, Tongji University, Shanghai, China. ²Institute of Pediatrics, Children’s Hospital of Fudan University, State Key Laboratory of Medical Neurobiology and MOE Frontiers Center for Brain Science, Institutes of Brain Science, Obstetrics and Gynecology Hospital of Fudan University and Department of Neurology, Huashan Hospital of Fudan University, Fudan University, Shanghai, China. ³Shanghai Tenth People’s Hospital, Institute for Infectious Diseases and Vaccine Development, Tongji University School of Medicine, Shanghai, China. ⁴Universidade de Vigo, Nutrition and Bromatology Group, Department of Analytical Chemistry and Food Science, Instituto de Agroecología e Alimentación (IAA) – CITE XVI, Vigo, Spain. ⁵Shanghai Universal Medical Imaging Diagnostic Center, Shanghai, China. ⁶Institute of Translational Medicine, Shanghai Jiao Tong University, Shanghai, China. ⁷Institute of Urban Agriculture, Chinese Academy of Agricultural Sciences, Chengdu National Agricultural Science and Technology Center, Chengdu, China. ⁸Institute of Neuroscience, CAS Center for Excellence in Brain Science and Intelligence Technology, University of Chinese Academy of Sciences, Chinese Academy of Sciences, Shanghai, China. ⁹Department of Neurosurgery, Children’s Hospital of Shanghai, Shanghai, China. ¹⁰Department of Neurosurgery, Hainan Women and Children’s Medical Center, Haikou, China. ¹¹These authors contributed equally: Chuantao Fang, Xiaodan Zhang, Lin Yang, Licheng Sun, Yujia Lu. ✉ e-mail: dr_zhaorui@sina.com; meixy@tongji.edu.cn; qidashi@fudan.edu.cn

only, and FCDIIb, which is marked by both CDN/BCs expressing both neuronal and glial proteins⁵.

The diversity and complexity of FCD make their pathogenesis challenging to fully elucidate⁹. Currently, the best-characterized etiology of FCDII malformations involves somatic variants in the mTOR pathway (e.g., *TSC2*, *AKT3*, *MTOR*, *DEPDC5*, *NPRL3*), which are considered a hallmark of these lesions^{10,11}. Hyperactivation of the mTOR pathway is frequently observed in FCDII, as evidenced by the pronounced activity of phosphorylated S6 in immunohistochemistry staining of the lesion neocortex^{11,12}. However, the mutational status of mTOR signaling is heterogeneous, both at the cellular and individual levels. For example, FCDII lesions are histologically characterized by the presence of CDN/BCs, which originate from distinct progenitor pools^{13,14}. Moreover, FCDII can occur in various regions of the brain neocortex, though it is most commonly found in the frontal lobes^{15,16}. These features of FCDII are not fully explained by the existing mTOR mutation theory, and genetic variations in mTOR signaling account for the pathogenesis of less than 50% of FCDII cases¹⁷. Therefore, a more detailed understanding of the cellular and molecular mechanisms contributing to FCD pathogenesis is crucial.

In this study, we employed single-nucleus RNA sequencing (snRNA-seq) to investigate cellular and molecular alterations in FCDIIb using samples from 15 patients across the prefrontal, temporal, and parietal neocortex. Pathological examination revealed pronounced vascular malformations and a distinct type of abnormal SMCs, termed ‘Firework cells’ (FCs), which had migrated into the brain parenchyma. These vascular abnormalities impair vessel function, creating ischemic-hypoxic (I/H) microenvironments that upregulate the HIF-1 α /mTOR/S6 pathway, disrupting neuronal and astrocyte activity and leading to neuronal loss. Additionally, zebrafish models confirmed that these I/H microenvironments can promote seizure activity. Our findings uncover cellular features of FCD, potentially aiding in diagnosis and treatment.

Results

Transcriptomic and cellular alternations in FCDIIb

To systematically investigate the cellular and molecular pathways underlying the etiology of FCDIIb, we performed unbiased snRNA-seq on 15 pairs of lesions and adjacent neocortical brain tissues from clinical cases. These samples included regions from 26 left prefrontal lobes, 2 temporal lobes, and 2 parietal lobes (Fig. 1a and Supplemen-

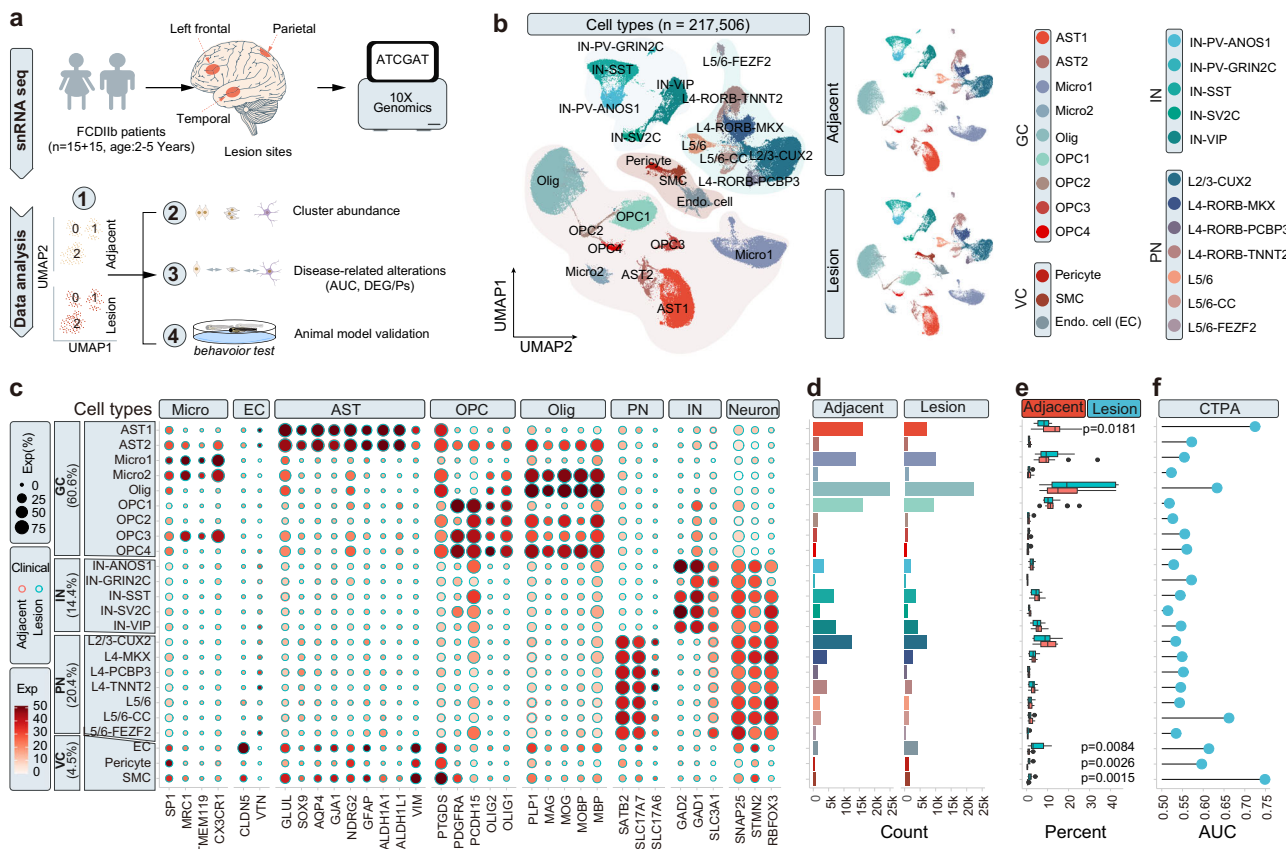


Fig. 1 | Overview of cell types in the Neocortex of FCDIIb Patients. **a** Schematic representation of experimental workflow of droplet-based snRNA-seq on FCDIIb neocortex biopsies using 10X genomics. A total of 15 pairs of lesion/adjacent brain neocortex samples were obtained from 15 FCDIIb patients. Red dots indicate the lesion sites. **b** UMAP visualization of snRNA-seq transcriptomic profiles from (a), showing the overall annotation of 24 major cell types. Different colors represent distinct cell types. IN interneuron, PN projection neuron, GC glial cell, VC vasculature cell, AST astrocyte, Olig oligodendrocyte, OPC oligodendrocyte precursor cell, SMC smooth muscle cell, EC endothelial cell; Micro microglia. **c** Dot plot illustrating the expression patterns of marker genes of Micro, EC, AST, OPC, Olig, and other cell types. Dot size represents the percentage of cells expressing each

gene in the indicated clusters, and color intensity reflects normalized expression levels. Clusters correspond to those in (b). **d** Descriptive statistics of the nucleus counts were obtained for each cluster in (b). The Cellular composition of the FCDIIb neocortex mainly consists of GC, PN, IN, and VC, closely resembling the normal neocortex³⁶. **e** Percentage of nuclei in each cluster in the snRNA-seq data. Lesion/Adjacent: lesion/adjacent neocortex of FCDIIb. $n = 15$. Data are presented as median (center line) with interquartile range (Q1-Q3, interquartile range, IQR), extending to $\pm 1.5 \times$ IQR from the box edges. P -value by two-tailed Wilcoxon matched-pairs signed rank test. Source data is provided as a Source Data file. **f** The AUC value from cell type prioritization analysis (CTPA) for each cluster. The Augur R package was used for CTPA, comparing lesion vs. adjacent conditions.

tary Data 1). The obtained snRNA-seq expression matrix underwent a rigorous quality control protocol, including 1) *in silico* correction for the potential ambient RNA contamination, 2) exclusion of cells with high mitochondrial gene expression (< 10% expression abundance), 3) filtering out cells with excessively low or high UMI counts (500–8000 in feature gene), etc (Supplementary Fig. 1a–c, 2a). Although the cell calling curve suggests that the quality of the S30 sample is relatively low, the overall sequencing quality remains acceptable (Supplementary Fig. 2a). Caglayan et al.^{18,19} highlighted that snRNA-seq data from the brain neocortex can be significantly affected by ambient RNA contamination (characterized by low *MALAT1* expression), which leads to distorted cell type annotations. In our dataset, all cells and samples demonstrated relatively balanced and acceptable *MALAT1* expression levels and ambient RNA contamination scores (Supplementary Figs. 2b, 3a). After these quality control steps, we finally obtained 217,506 single-nucleus transcriptional profiles, comprising 112,321 nuclei from adjacent neocortex and 105,185 nuclei from lesion sites (Fig. 1b and Supplementary Data 2). Overall, the cells from both adjacent and lesion neocortex regions exhibited comparable high-quality metrics, with an average of 3202 detected genes in adjacent sites and 3023 in lesion sites (Supplementary Data 2).

Leveraging independent postnatal human neocortex snRNA-seq datasets^{19–22}, we annotated the unsupervised clusters, totaling over 150, using a reference-based algorithm implemented in the Clustify R package²³, followed by manual correction of inconsistent or ambiguous clusters based on feature markers and enriched pathways (Fig. 1b and Supplementary Data 3, 4). This approach categorized the cells into 24 major clusters, including 7 projection neuron clusters, 5 interneuron clusters, 9 glial cell clusters, and 3 vascular cell clusters (Fig. 1b, c). The resulting neuron-to-glia ratio was approximately 1:1.7²⁴, with neurons constituting 34.8%, glial cells 60.6%, and vascular cells 4.5% of the total cell population (Fig. 1c). All cell types displayed balanced and satisfactory quality metrics regarding mitochondrial gene content, UMI count, and ambient RNA abundance (Supplementary Fig. 3b)¹⁸. Despite the overall high quality, we observed considerable variability within an acceptable range in the number of each cell type among individuals (Supplementary Fig. 3c), which may be attributed to the heterogeneous structure of the neocortex in FCDIIb patients or technical factors. Similar variations in cell cluster numbers have been reported in other studies^{21,25}. Importantly, cell types from both lesion and adjacent regions were accurately identified using established markers and exhibited similar distributions in cell numbers (Fig. 1c, d), underscoring their overall comparability.

Comparative analysis of cell type abundance between the lesion and adjacent neocortex revealed significant differences particularly in SMCs, endothelial cells, pericytes, and astrocytes (Fig. 1e). To further assess the contribution of each cell type to the pathogenesis of FCDIIb, we conducted cell type prioritization analysis using the Augur R package²⁶. This analysis assigns an area under the receiver operating characteristic curve (AUC) value to each cell type to estimate overall variation between conditions, in this case, lesion versus adjacent neocortex. Interestingly, astrocytes and SMCs exhibited the highest AUC values, indicating the most significant transcriptomic variations between the lesion and adjacent regions (Fig. 1f). Collectively, this comprehensive dataset provides valuable insights into the molecular and cellular manifestations of FCDIIb, offering a robust resource for further exploration of its pathogenesis.

Vascular aberration as a dominant feature of the neocortex in FCDIIb lesions

Given the complexity and heterogeneity of the human brain neocortex, we performed multi-dimensional scaling (MDS) analysis on our snRNA-seq dataset to assess the impact of potential confounding factors, such as neocortex region and age. We found that the variations

sourced from these factors were minor (Supplementary Fig. 4a). Additionally, the relative proportions of identified clusters showed significant variation but no distinguishable difference among neocortex regions (Supplementary Fig. 4b), suggesting that these factors can be considered negligible. Consequently, we conducted differential state (DS) analysis to identify cell-type-specific differentially expressed genes (DEGs) in response to FCDIIb (lesion vs. adjacent) using the Muscat R package²⁷. Glial and vascular cells, such as astrocytes and SMCs, exhibited significant aberrations under clinical conditions in DS analysis ($|\log_2\text{fold change}| > 1.5$, $p\text{-value} < 0.05$), some of which are epilepsy-associated genes in GWAS studies²⁸ (Fig. 2a, Supplementary Fig. 4c and Supplementary Data 5). Functional enrichment analysis of these DEGs revealed alterations in SMCs related to cell migration, mechanoreceptor differentiation, etc (Fig. 2b and Supplementary Data 6). In astrocytes, aberrations were frequently observed in pathways involved in blood vessel development/morphogenesis, vasculature development, and neuron projection (Supplementary Data 6). These findings suggest potential roles for non-neuronal cells in the pathogenesis of FCDIIb.

Next, we evaluated the relationship between cell clusters and disease using a gene set variation analysis (GSVA)-based differential pathway analysis, utilizing well-defined disease/phenotype-related gene sets from DisGeNet (<http://www.disgenet.org>), Disease Ontology (DO, <https://disease-ontology.org>), Human Phenotype Ontology (HPO, <https://hpo.jax.org>), and other sources^{29,30}. SMCs were significantly associated with 55 nervous system diseases and 16 mental disorders, accounting for 7.5% of all disease-associated terms in DisGeNet (Fig. 2c and Supplementary Data 7). Meanwhile, pathways associated with seizures and epilepsy were also significantly altered in vascular cells, including SMCs (25), pericytes (15), endothelial cells (13), and astrocytes (24) (Fig. 2d and Supplementary Data 8). Similarly, 6.3% and 2.9% of differentially expressed pathways (DEPs) in astrocytes were associated with these two categories of diseases, respectively (Supplementary Data 7). Additionally, astrocytes were linked to abnormalities in nervous system morphology (e.g., cerebellar cortex, brain, neurons), vascular degeneration, and abnormal blood vessel morphology (Supplementary Data 7). Together with DEG-based analysis, all these findings strongly suggest that aberrations in vascular cells and astrocytes may be linked to FCDIIb.

To gain a deeper understanding of the molecular events disrupted in the lesion neocortex, we performed GSVA to identify signaling pathways whose alterations may underlie the etiology of FCDIIb. The number of DEPs was fairly consistent across clusters (Supplementary Fig. 4d and Supplementary Data 9). Notably, astrocytes and endothelial cells exhibited alterations in signaling pathways associated with cellular responses to vascular endothelial growth factor stimulus, positive regulation of vasculogenesis, vascular endothelial cell proliferation, and vasculature development (Supplementary Data 9). Additionally, hypoxia-related pathways were significantly modified in almost all cell types, highlighting changes in vascular functions or oxygen supply in the neocortex of FCDIIb (Supplementary Data 9). These results suggest that various vascular abnormalities may be present in the neocortex of FCDIIb lesions. Consistent with these findings, Hematoxylin-Eosin (HE) staining revealed a much higher frequency of vascular system malformations, including endothelial cell proliferation, vessel thickening, infarction, and fibrosis in the FCDIIb and FCDIIb with mTOR variants lesion neocortex sections (Fig. 2e and Supplementary Fig. 4e). Consistently, Western blotting results also indicated that the expression level of SMC markers (e.g. TAGLN) was aberrantly altered, being associated with CDN/BCs marker (VIM) (Supplementary Fig. 4f). Collectively, these results demonstrate that molecular and morphological alterations in vascular cells are key features of the FCDIIb lesion neocortex.

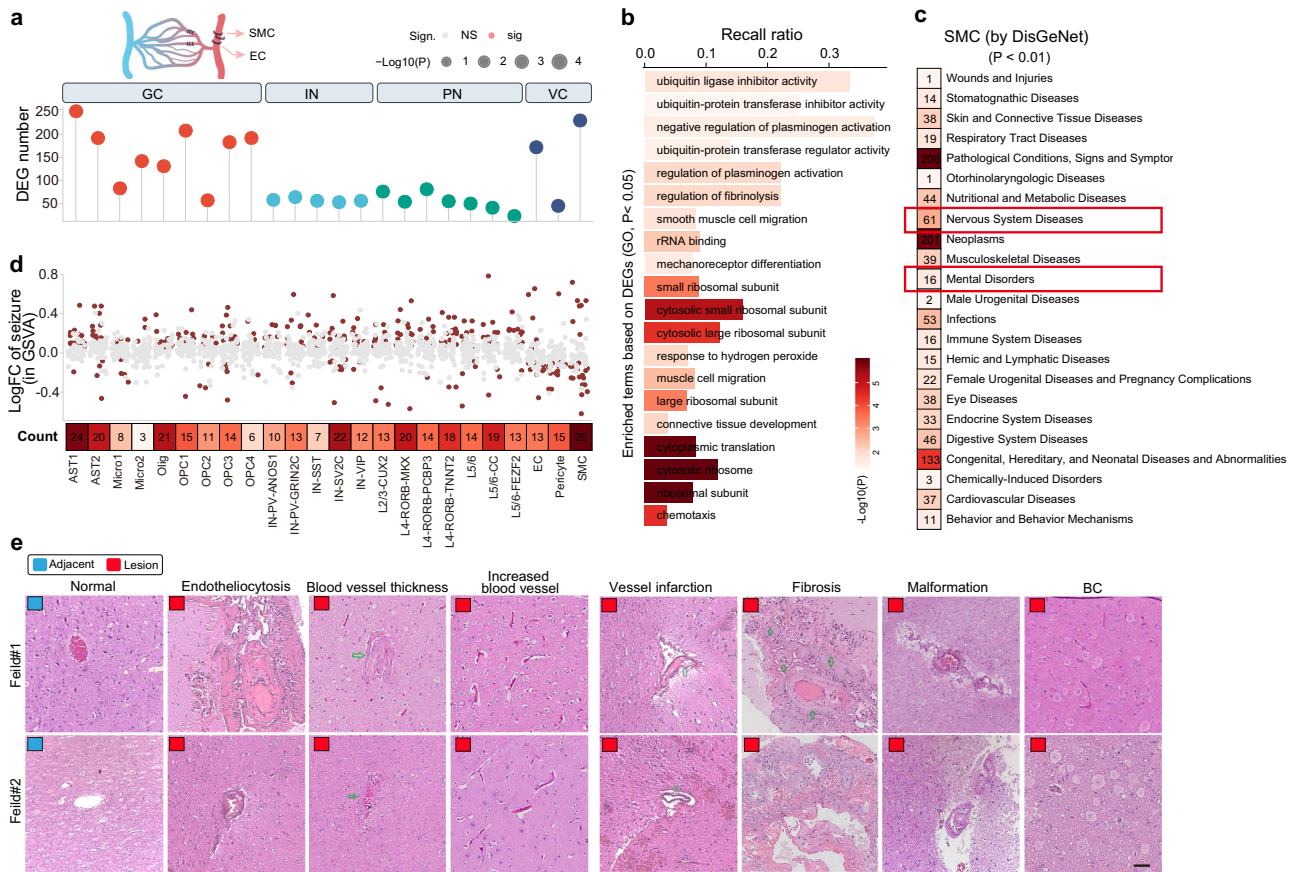


Fig. 2 | Vasculature aberration is a dominant feature of the neocortex of the FCDIIb lesions. **a** Differentially expressed genes (DEGs) in each cluster when comparing lesion and adjacent neocortex. DEGs were identified by differential state analysis, with a cutoff of $|\log_2$ fold change > 1.5 and P -value < 0.05 . P -value was defined by the limma-voom-based method using the Muscat R package. IN interneuron, PN projection neuron, GC glial cell, VC vasculature cell. **b** Top 20 of DEG-based enriched gene ontology (GO) terms of SMCs. DEGs from (a) were used for enrichment analysis with a cutoff p -value < 0.05 . P -value was defined by the Hypergeometric test using the Gprofiler2 R package. **c** Statistics of SMC-related human diseases. Significant terms were defined by pathway-based differential analysis based on the Empirical Bayes method using the Limma R package, with a

cutoff of p -value < 0.01 . The pathway enrichment score for DisGeNet gene sets was calculated using the GSVA algorithm. **d** Differentially expressed pathways (DEPs) in clusters from Fig. 1b using seizure/epilepsy-related gene sets. The GSVA algorithm was employed to transform the pseudo-bulk expression matrix into a pathway matrix. DEPs were identified using the Limma R package with a cutoff p -value < 0.05 . The heatmap indicates the total number of DEPs. DEPs were defined by the Empirical Bayes method using the Limma R package. **e** Representative histological features of neocortexes as determined by HE staining. Each experiment was repeated independently 3 times. Normal/Lesion; adjacent/lesion neocortex of FCDIIb; arrows indicate typical features; scale bar, 50 μ m.

Firework cells: abnormal SMCs in FCDIIb lesions

SnRNA-seq and HE staining results revealed that vascular malformation is a prominent pathological feature of FCDIIb, particularly in the SMCs. In molecular ontology, we observed that a large number of altered pathways in SMCs were significantly associated with abnormal cell morphology, cell differentiation, cytoskeleton, migration, etc (Supplementary Fig. 5a and Supplementary Data 10). To confirm our analysis results, we re-analyzed the bulk RNA sequencing data from the FCDII neocortex using two independent algorithms: CIBERSORTx³¹ and Granulator³². Importantly, the percentage of SMCs in FCDII, particularly FCDIIb, was significantly higher than in the control neurotypical neocortex (Supplementary Fig. 5b), consistent with our snRNA sequencing results. Furthermore, we aligned our data with other 4 PFC snRNA-seq data, and observed that a fraction of the SMC population was only enriched in FCDIIb cortices (Supplementary Fig. 5c).

To further investigate these vascular abnormalities, we performed immunofluorescence (IF) staining for ACTA2 and PDGFA to visualize the SMCs and vascular cells in the FCDIIb lesion brain tissues (Fig. 3a). We observed a type of abnormal SMCs that migrated from blood vessels into the brain parenchyma (Fig. 3a and Supplementary Fig. 5d). These cells were characterized by extensive, fluffy processes

resembling firework-like patterns, and, therefore, we termed them firework cells (FCs) (Fig. 3a and Supplementary Fig. 5d). We also identified this type of abnormal SMCs in samples with mTOR variants (Supplementary Fig. 6a–e). The phenotype of FCs probably is explained by the pathway-level alterations of SMCs mentioned above (Supplementary Fig. 5a). In spatial location, FCs are primarily scattered around arterioles and show very few intersections with endothelial cells (Fig. 3a), which, however, are unlike normal SMCs.

To ensure that FCs were not misidentified as astrocytes or neurons, we performed IF staining using different SMC markers (ACTA2 and TAGLN) with well-established astrocyte (GFAP) or neuron (NeuN) markers. In the staining images, we found no overlapping signals between SMC and astrocyte/neuron markers (Fig. 3b). Anatomically, SMCs are tightly wrapped around blood vessels in adjacent normal brain neocortex, while astrocytes were positioned around the vessels (Supplementary Fig. 5e), consistent with previous reports^{33,34}. These results indicate the good specificity of our IF staining experiments. We observed that both FCs and astrocytes extensively proliferated in the lesion area of FCDIIb (Fig. 3b and Supplementary Fig. 5d). More interestingly, numerous FCs were observed detaching from the blood vessels and migrating into the brain parenchyma,

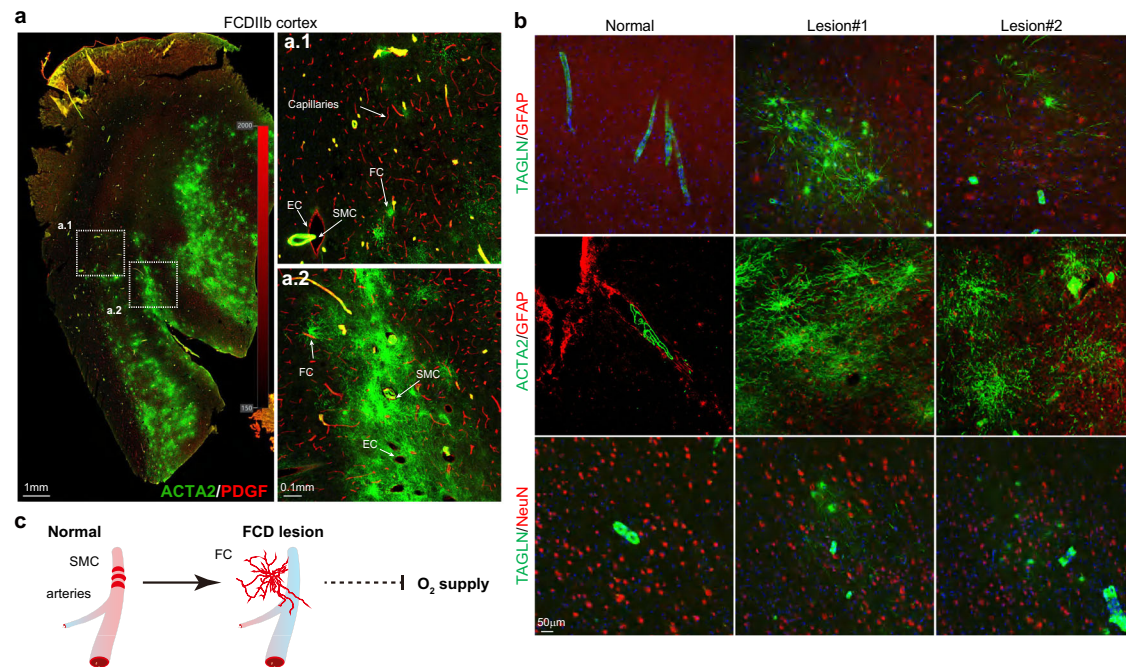


Fig. 3 | Firework cell: abnormal SMCs in FCDIIb. **a** Immunofluorescence (IF) staining for PDGF (red)/ACTA2 (green) in lesion neocortex sections of FCDIIb patients. The dashed square indicates a local magnification. Scale bar, 1 and 0.1 mm. **b** IF staining for GFAP (red), TAGLN (green), and ACTA2 (green) in neocortex sections from FCDIIb patients and the paired adjacent neocortex. Scale bar,

0.1 mm. **c** Schematic model representing vascular system aberration in lesion neocortex. SMCs detach from endothelial cells to form FCs, impairing the contractile function of blood vessels and reducing oxygen supply. FC firework cell, SMC smooth muscle cell.

leading to a reduction in normal SMCs on the vessels (Fig. 3a and Supplementary Fig. 5d–g). In contrast, the morphology and number of astrocytes surrounding the blood vessels in the lesion area showed no significant changes compared to normal regions (Fig. 3b and Supplementary Fig. 5e–g). Meanwhile, IF staining of TAGLN also produced similar results (Supplementary Fig. 5h). Besides, The quantification shows that the diameter of FCs is approximately 260 μm , which is at least 10 times larger than the 27 μm diameter of astrocytes (Supplementary Fig. 5i). All these findings demonstrate that FCs are distinct from astrocytes and neurons. To explore the molecular cues that might contribute to the aberrant morphology of FCs, we compared the lesion and adjacent SMCs populations and found genes including *NR4A3*, *CTNNA1*, and *CRISPLD2* significantly upregulated in lesion sites (Supplementary Fig. 5j). Additionally, overexpression of *CTNNA1* and *CRISPLD2* induced slight morphological changes (including cell spreading and the extension of axon-like tentacles) for cells (Supplementary Fig. 5k), being reminiscent of the morphology of FCs.

Typically, SMCs encircle endothelial cells to regulate blood flow in the brain neocortex, and morphological changes in these cells can lead to functional impairments in various diseases, such as cerebral ischemia³⁵. In the lesion neocortex of FCDIIb, the occurrence of FCs obviously impairs the function of blood vessels due to the loss of normal SMCs. Indeed, we found extensive alterations of hypoxia-related pathways among almost all cell types (Supplementary Data 9). Therefore, the presence of FCs in the lesion neocortex may contribute to localized inefficiencies in oxygen supply or create a hypoxic environment (Fig. 3c), representing another characteristic of FCDIIb.

Local ischemia-hypoxia: the pathogenic contribution of vascular malformation

These results above suggest that FCDIIb patients may experience local I/H microenvironments in the lesion brain areas due to vascular malformations. Clinical imaging analysis of a large cohort of FCDIIb patients using arterial spin labeling (ASL) perfusion and positron

emission tomography-computed tomography (PET-CT) MRI revealed significantly reduced blood flow and low metabolic characteristics in the lesion brain areas (Fig. 4a), typical features of cerebral ischemia. These findings were consistent with those observed in samples with mTOR variants (Supplementary Fig. 6f). To further validate the presence of I/H, we performed HIF-1 α IF staining. This staining showed that HIF-1 α ⁺ cells scattered around FCs but not normal vessels (Fig. 4b). Additionally, co-IF staining of HIF-1 α and the FCDII marker VIM revealed that many VIM⁺ cells in the lesion neocortex highly expressed HIF-1 α (Fig. 4b). These findings collectively support the hypothesis that severe vascular malformations in the FCDIIb lesion brain areas lead to local I/H microenvironments.

The effects of such local I/H microenvironments in the lesion neocortex are likely to 1) alter the activity of local astrocytes, thereby disrupting neuronal function, or 2) directly impair neurons. DEP analysis indicated significant gene alterations in astrocytes, which are closely associated with seizures and epilepsy (Fig. 2d and Supplementary Data 8). In CTPA, astrocyte populations showed an AUC of 0.74 (Fig. 1f), indicating a notable distinction between lesions and adjacent tissues. At the pathway level, signaling pathways associated with astrocyte activation, such as Calcium, Cytokine-related, and JAK-STAT signaling pathways, were notably altered in astrocytes³⁶ (Supplementary Data 11), highlighting their significant activation changes. Therefore, we also conducted IF staining against the astrocyte marker GFAP. Interestingly, we found that astrocytes were unevenly distributed around blood vessels in an island-like pattern in FCDIIb lesions, which we referred to as astrocytic island (Fig. 4c). However, astrocytic islands were not present in adjacent neocortex sections (Fig. 4c), suggesting different activation statuses of astrocytes between the lesion and adjacent areas. These findings collectively emphasize that the alteration of astrocyte activity or the occurrence of astrocytic islands is another feature of FCDIIb.

Analysis of neuron numbers in FCDIIb lesion areas showed a significant neuronal loss in FC⁺ regions compared to normal areas, as

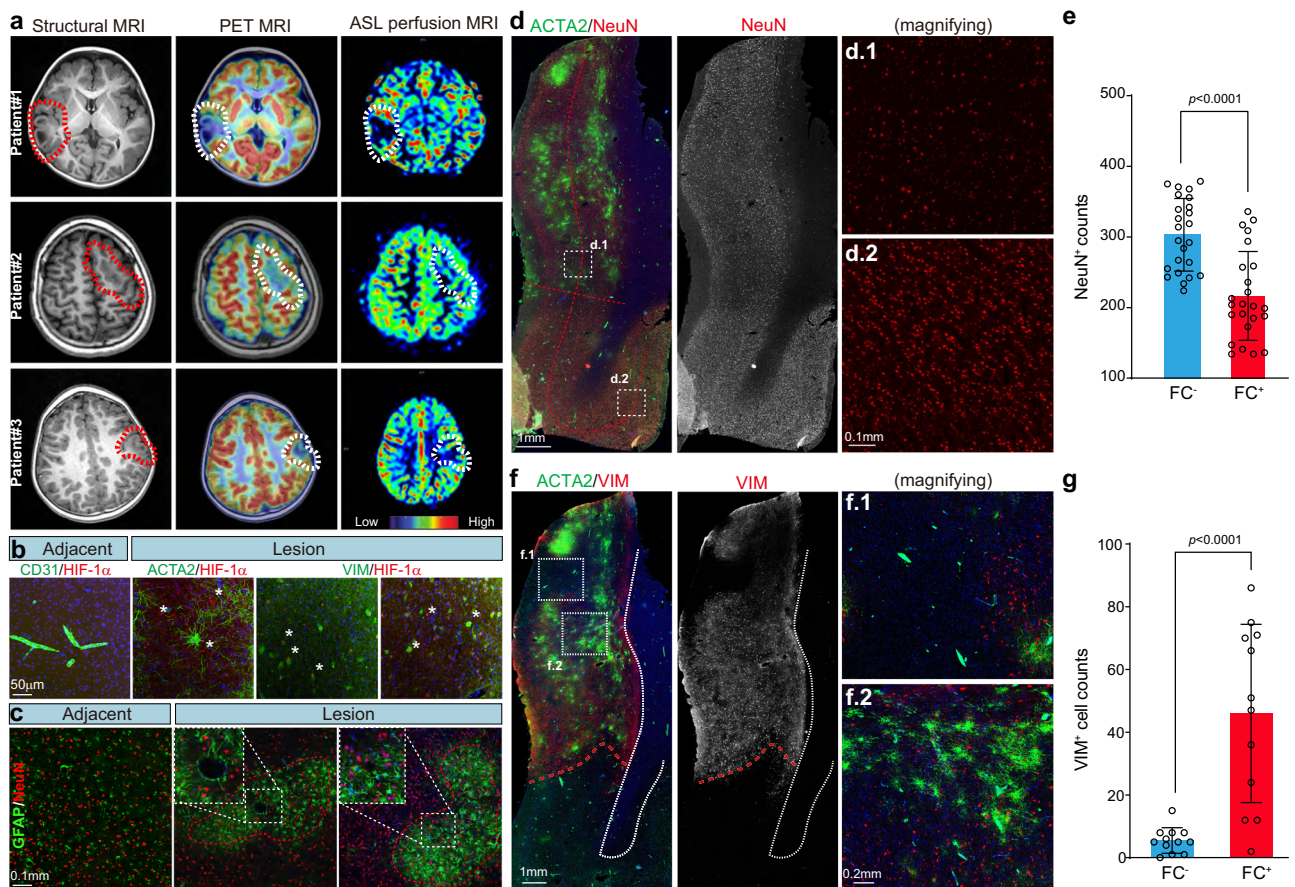


Fig. 4 | Local ischemia-hypoxia: the pathogenic contribution of vascular malformation. **a** Imaging presentations showing the lesion sites in FCDIIb patients. MRI reveals focal cortical dysplasia, including cortical malformation, thickened neocortex, and blurred gray and white matter interface. PET/MRI images show focal hypometabolism in the lesion area. ASL perfusion MRI demonstrates a focal decrease in cerebral blood flow in the lesion area. **b** Immunofluorescence (IF) staining for CD31, ACTA2, VIM, and HIF-1 α in the lesion and adjacent neocortex sections of FCDIIb patients. The asterisk indicates HIF-1 α ⁺ cells. Each experiment was repeated independently 3 times. **c** IF staining for GFAP (green) and NeuN (red) in neocortex sections of FCDIIb patients. GFAP-labeled astrocytes form a typical astrocytic island (red dashed circle). The dashed square indicates a local magnification. **d** IF staining for ACTA2 (green) and NeuN (red) for neocortex sections of FCDIIb patients. The dashed square indicates a local magnification. The red dashed curve indicates the boundary between the low and deep layers. **e** Statistical analysis

of the impact of FCs presence on neuron count. The number of neurons in FC⁺ regions is significantly lower compared to FC⁻ regions. FC⁻, FC negative/positive region. The neuron number of 24 independent local sites (1 \times 1 mm²) was counted. Data are presented as mean \pm SD. *P*-value < 0.0001 by two-sided Student's *t*-test. Source data is provided as a Source Data file. FC, firework cell. **f** IF staining for ACTA2 (green) and VIM (red) in lesion neocortex sections of FCDIIb patients and associated statistics. The dashed square indicates a local magnification. The red dashed curve indicates the boundary between the lesion and adjacent areas. **g** Statistical analysis of the impact of FCs presence on VIM⁺ cell count. Regions with a higher number of FC⁺ cells show a significantly greater number of VIM⁺ cells compared to regions with fewer FC⁺ cells. The neuron number of 12 independent local sites (2 \times 2 mm²) was counted. Data are presented as mean \pm SD. *P*-value < 0.0001 by two-sided Mann-Whitney nonparametric test. Source data is provided as a Source Data file. FC firework cell.

evidenced by IF staining of NeuN and ACTA2 (Fig. 4d, e). Meanwhile, high VIM levels were also observed in FC⁺ areas compared to normal regions (Fig. 4f, g). Thus, vascular malformations causing I/H micro-environments in FCDIIb lesions may represent a key pathological mechanism underlying the development and progression of this disorder.

Vascular malformation pathogenically contributes to seizure

Previous studies have identified somatic variants (e.g., *TSC2*, *AKT3*, *MTOR*, etc) in the mTOR or related pathways in projective neurons within the lesion neocortex¹⁰. However, the activity of these pathways was extensively altered in astrocytes, SMCs, and interneurons, in addition to projective neurons (Supplementary Data 9). To validate these findings, we performed IF staining for CD31 and phosphorylated S6 (Fig. 5a). We found that pS6 signals were frequently found in SMCs and pericytes, which are also highly associated with the distance to lesion sites in neocortex sections (Fig. 5a). More interestingly, IF

staining for ACTA2 and pS6 revealed a strong association between the distribution of FCs and pS6 in FCDIIb lesion (Fig. 5b, c). This result was similarly observed in samples from patients with mTOR variants (Supplementary Fig. 6a–e). In Western blot analysis, pS6 levels in the lesion neocortex were significantly upregulated in FCDIIb patients, showing a 2.3-fold increase compared to adjacent neocortex areas (Fig. 5d). These data collectively elicit that vascular malformation is tightly linked to mTOR activity.

Extensive research has shown that VIM⁺ CDN/BCs are primarily a category of projective neurons³⁷. However, our study indicates that they originate from diverse progenitor sources, including caudal ganglionic eminences (SP8), medial ganglionic eminence (SOX6), and cortical regions (CUX1 and CTIP2) (Supplementary Fig. 7a), inconsistent with previous observations^{1,38}. In theory, these findings can be explained by activity aberration rather than only genetic mutations in the mTOR pathway in FCDII, because the latter is limited to cell types and spatial distribution in the context of the brain. To further explore

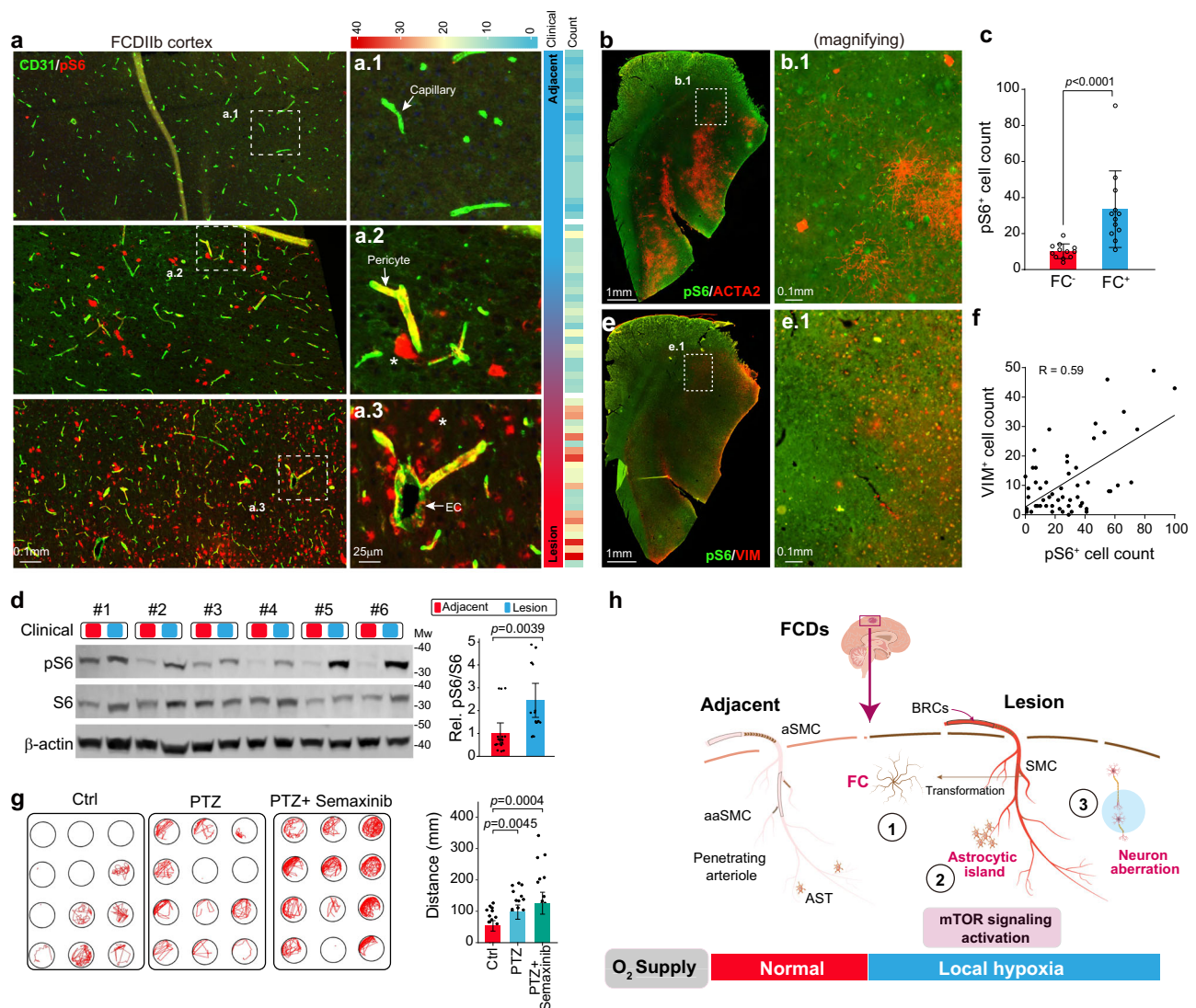


Fig. 5 | Vascular malformation contributes to seizure pathogenesis.

a Immunofluorescence (IF) staining for CD31 and pS6 for neocortex sections of FCDIIb patients. The right panel shows a local magnification of the sections within the dashed box. EC, endothelial cell. **b, c** IF staining for ACTA2 and pS6 (**b**) in lesion neocortex sections from FCDIIb patients and corresponding statistics (**c**). The cell number of 12 independent local sites ($1 \times 1 \text{ mm}^2$) was counted. Data are presented as mean \pm SD. P -value < 0.0001 by two-sided Mann-Whitney nonparametric test. Source data is provided as a Source Data file. FC, firework cell. **d** Western blot analysis of the indicated protein pS6 and S6 expression levels in the neocortex of FCDIIb patients. Both lesion and paired adjacent neocortex samples were used. pS6: phosphorylated S6 protein. $n = 18$. Data are presented as mean \pm SD. P -value = 0.0039 by two-sided paired t -test. Mw, molecular weight. Source data is provided as a Source Data file. **e, f** IF staining for ACTA2 and VIM (**e**) in lesion

neocortex sections from FCDIIb patients and associated statistics (**f**). The cell number of 54 independent local sites ($1 \times 1 \text{ mm}^2$) was counted. P -value < 0.0001 of linear regression by F-test; R , Pearson correlation coefficient. Source data is provided as a Source Data file. **g** Behavioral testing of the improvement in PTZ-induced seizure activity in zebrafish treated with Semaxinib. PTZ pentylenetetrazole. $n = 24$. Data are presented as mean \pm SD. P -value by two-sided Mann-Whitney nonparametric test. Source data is provided as a Source Data file. **h** Schematic model of how vascular malformation contributes to seizure pathogenesis. In the lesion region, these FCs fail to encircle endothelial cells as normal SMCs do, depleting the SMC pool and impairing the contractility of vessels (including arteries and arterioles SMC). This leads to the creation of a local hypoxia environment within the lesion neocortex, which, along with mTOR activation, further disrupts astrocyte and neuron functions. AST astrocyte, aSMC arteries SMC, aaSMC arterioles SMC.

whether elevated mTOR pathway activity is pathogenic in FCDIIb lesions, we co-stained FCDIIb neocortex sections with pS6 and VIM. Intriguingly, our results showed a partial overlap of pS6 signals with a strong association with VIM (Fig. 5e, f), indicating that mTOR pathway aberrations are pathogenic to both interneurons and projection neurons in FCDIIb lesions (Supplementary Fig. 7b). Additionally, signaling pathways related to action potentials, AMPA/glutamate receptors, cation channels, and synaptic vesicles were significantly altered in projection neurons (Supplementary Data 12), which is consistent with changes in seizure-related pathways (Fig. 2a, b). To provide further evidence of the pathological role of vascular abnormalities in FCDIIb,

we pre-treated zebrafish with Semaxinib, a VEGFR inhibitor that induces vascular hypoplasia³⁹. We observed that Semaxinib treatment significantly exacerbated the pentylenetetrazole-induced seizure phenotype in zebrafish models (Fig. 5g). Altogether, these findings indicate that vascular malformation pathogenically contributes to seizure.

Discussion

Extensive investigations have highlighted the heterogeneous nature of FCD in both clinical features and molecular etiology, complicating the understanding of their underlying pathogenesis. While single

causative germline and somatic gene mutations in the mTOR signaling pathway (e.g., *MTOR*, *DEPDC5*, and *NPRL3*) are frequently observed in FCDIIb cases, they are rarely identified in FCD-I/III^{39,40}. Although Rapamycin (a mTORC1 inhibitor) is frequently used to reduce seizure frequency in epileptic rodent models⁴¹, clinical outcomes with mTOR inhibitors in treating FCD are suboptimal⁴². Therefore, a broader perspective is necessary to systematically investigate the molecular events involved in FCDII development. Our findings reveal that significant aberrations in FCDIIb are primarily in the vascular system and glial cells, particularly SMCs and astrocytes. HE staining revealed frequent vascular malformations, such as endotheliocytosis and vessel thickening, in FCDIIb cortices. IF staining identified a distinct type of abnormal SMCs, termed FCs, which migrate from blood vessels into the brain parenchyma. Notably, VIM⁺ abnormal neurons and pS6⁺ cells were associated with the distribution of these FCs in the lesion neocortex. Collectively, these findings demonstrate that vascular aberrations and FCs are critical features of FCDIIb.

A local hypoxic environment in the neocortex is well-recognized as being closely linked to epilepsy, with neonatal hypoxic-ischemic encephalopathy serving as a classic example⁴³. Intracranial vascular malformations, including cavernous hemangiomas, arteriovenous malformations, developmental venous anomalies, and capillary telangiectasias, are also significant causes of epilepsy^{44–46}. Consequently, hemorrhage or ischemia resulting from these vascular malformations within the brain is a major trigger for clinical seizure occurrences. Our study integrates snRNA-seq results, pathological examinations, and IF staining to underscore the critical role of vascular aberrations and FCs in FCDIIb. Moreover, previous reports, such as those by Hildebrandt et al. in 2008, have highlighted the presence of spongiform white matter angiopathy in patients with chronic epilepsies, resembling our observations in FCDII⁴⁷. Additionally, recent studies by Shen et al. have indicated elevated expression of vascular endothelial growth factor-C and its receptors in epileptic lesions of patients with tuberous sclerosis complex epilepsy⁴⁸. Collectively, these findings suggest that vascular abnormalities leading to brain ischemia or hemorrhage may represent an additional pathogenic mechanism of FCDII. Our observations of reduced blood flow and hypometabolic states at the lesion sites of the FCDIIb neocortex, along with typical glial proliferation, neuronal loss, and upregulation of HIF-1 α expression, support the hypothesis that I/H microenvironments may serve as another pathogenic mechanism of FCDIIb. Zebrafish models of vascular malformation further confirm that these abnormalities can promote epilepsy. These insights underscore the importance of understanding the vascular component in the pathogenesis of FCDII and offer potential avenues for target therapeutic interventions.

Mutations in mTOR pathway-related genes have been identified in the FCDII lesion neocortex, particularly in CDN/BCs, which are now considered mTORopathies^{49,50}. These mutations are believed to induce the seizure phenotype in humans by increasing neuronal excitability directly and disrupting cell migration in a non-cell-autonomous manner, causing cortical dyslamination⁵⁰. However, CDN/BCs originate from distinct progenitor pools, and their low detection frequency further indicates that there are additional mechanisms of mTOR activation in FCDII. Hypoxia has been extensively demonstrated as a critical cue to induce the activation of mTOR signaling⁵¹. In the local field of the FCDIIb neocortex, vascular malformation characterized by FCs, which fail to form rings around endothelial cells like normal SMCs, detach from blood vessels, and migrate into the brain parenchyma, exhausts the SMCs pool. This leads to the loss of overall contractility in vessels and a local ischemia/hypoxia environment. Consequently, this effect impacts surrounding cells such as glial cells, vascular cells, and neurons in the lesion neocortex, leading to alterations in mTOR signaling (Fig. 5h). Indeed, our analysis revealed that mTOR signaling was significantly altered in the vascular cells, neurons, and astrocyte. Consistently, IF staining also

showed a large number of mTOR-activated blood vessels, which were also associated with the distribution of FCs in the lesion neocortex. In IF staining for the FCDIIb lesion neocortex, VIM⁺ abnormal neurons were also associated with pS6⁺ cells in distribution. Furthermore, the number of neurons surrounding FCs was significantly reduced. These observations suggest that vascular abnormalities are another contributor to the aberration of mTOR signal activity in FCDIIb.

In conclusion, our study reveals that vascular system disorder-induced hypoxia and mTOR activation may also provide a pathological mechanism for FCDIIb. Our study identifies vascular malformation and FCs as other features or notable risk factors for FCDIIb, emphasizing a promising approach to address this brain developmental disorder.

Methods

Human brain samples

The collection of human brain samples was approved by the Ethical Committee of the Children's Hospital of Fudan University (IRB 2021-77), and written informed consent was obtained from the patient's legal guardians or authorized representatives. The human brain samples used in this study were obtained from 35 patients diagnosed with FCD, with ages ranging from 0 to 5 years. Clinical information and sex details are provided in Supplementary Data 1. All patients underwent surgical intervention following the identification of the epileptogenic zone through electroclinical data and clinical imaging evaluations, including structural MRI, Arterial Spin Labeling (ASL) MRI, and PET/MRI. The lesion sites in the neocortex were accurately localized, and En bloc resections were planned preoperatively to minimize the risk of postsurgical deficits.

snRNA sequencing and data processing

Single nucleus 3' gene expression profiling was performed by Shanghai Applied Protein Technology Co. Ltd., (Shanghai, China) using Chromium Next GEM Single Cell 3' Kit v3.1 (10X Genomics, 1000268) and Chromium Next GEM Chip G Single Cell Kit (10X Genomics, 1000120). The nucleus suspension was loaded onto the Chromium single-cell controller (10X Genomics) to generate single-cell gel beads in the emulsion according to the manufacturer's protocol. Captured nuclei were lysed and the released RNA was barcoded through reverse transcription in individual GEMs. Cell-barcoded 3' gene expression libraries were sequenced on an Illumina NovaSeq6000 system.

Cell Ranger software (v.4.0.0) (10X Genomics) was utilized for aligning the clean reads to the Homo sapiens (assembly GRCh38.p14) and gene counting with the default parameters, using the officially prepared reference downloaded by <https://cf.10xgenomics.com/supp/cell-exp/refdata-gex-GRCh38-2020-A.tar.gz>. To remove the potential ambient RNA contamination, three independent algorithms including Cellbender⁵², DecontX⁵³, and SoupX⁵⁴ were employed following their manual vignettes. Briefly, the alignment file named "possorted_genome_bam" in the Cell Ranger output directory was subjected to Cellbender, using a sub-command of remove-background with parameters of --expected-cells 10000 and --epochs 100. Then, obtained filtered output files were further cleaned out ambient RNA contamination in the R language platform using packages of DecontX and SoupX following the default settings. Meanwhile, doublets and multiplets in the data matrix were predicted using DoubletFinder (<https://github.com/chris-mcginnis-ucsf/DoubletFinder>) and scDblFinder (<https://github.com/plger/scDblFinder>), and the intersection of two different predictions was filtered out from the data matrix.

The obtained high-quality expression matrix was used to identify different clusters and signature genes employing the famous R package Seurat (v4.1.1, <https://satijalab.org/seurat/>) following the official tutorials. First, we filtered out the relatively high-quality single nuclei

by a cut-off of 500–8000 feature genes and mitochondrial percent <10%. After these filtering steps, 217,506 high-quality single-nuclei transcriptional profiles were obtained, and the separated data matrix of each neocortex sample was integrated using the R package Harmony (<https://github.com/immunogenomics/harmony>), a fast, sensitive, and accurate integration algorithm for single-cell dataset⁵⁵. After reduction using top30 principal component in PCA, the integrated dataset was represented using two-dimensional Uniform Manifold Approximation and Projection (UMAP) space, and the un-supervised clusters were identified sequentially using FindNeighbors and FindClusters (at 1.0 resolution). For the biological annotation of each cluster, R package Clustifyr (<https://bioconductor.org/packages/release/bioc/html/clustifyr.html>) was used with 3 independent references based on the expression matrix of Velmeshev et al.⁵⁶, Pfisterer et al.⁵⁷ and Yang et al.²² for neurons, glial cells, and vasculature cells, respectively. Finally, the annotated clusters were manually refined using the well-validated cell type markers and pathways, for instance, inhibitory neuron types: *GADI2*, *PVALB*, *SST*, *VIP*, and *SV2C*; excitatory neurons: *SYT1*, *RBFOX3*, *CUX2*, *SATB2*, *RORB*, and *TLE4*; glia cells: *SLC1A2*, *GAFP*, *PLP1*, *PDGFRA*, and *PTPRC*; vascular cells: *CLDN5*.

Differential expression gene and pathway analysis

Cluster marker genes were identified using the FindAllMarkers function in Seurat with the Wilcoxon Rank Sum test, and parameter settings of $pct.1 > 0.6$ and $pct.2 < 0.4$ were used to filter, and all the obtained markers were subjected to gene set enrichment to validate the cell type annotation. To identify gene aberration in response to disease status, we carried out pseudo-bulk RNA sequencing (RNA-seq) differential expression gene (DEG) analysis using an R package Muscat: multi-sample multi-group scRNA-seq analysis tools⁵⁴, which aggregates single nucleus signals across cell type and clinical factors. DEGs were considered based on the cutoff of absolute $avg_logFC \geq 1.5$ and $p\text{-value} < 0.05$.

The metacell expression count matrix calculated by muscat of each cluster was transformed to TPM (transcripts per million) matrix using a function of count2tpm from the IOBR package (<https://github.com/IOBR/IOBR>), which was further used to calculate pathway matrix using the gsva function in the GSVA R package (<https://www.bioconductor.org/packages/release/bioc/html/GSVA.html>) with gene sets defined by the latest GO (Gene Ontology), KEGG (Kyoto Encyclopedia of Genes and Genomes), Panther, PFOCR (Pathway Figure OCR), Reactome, WikiPathways, Human MSigDB Collections, HPO (Human Phenotype Ontology), etc. Differential expression pathway (DEP) analysis was carried out for the pathway matrix of each cluster using the limma R package (<https://bioconductor.org/packages/release/bioc/html/limma.html>). DEPs were considered based on the cutoff of $p\text{-value} < 0.01$. The significant terms in gene set enrichment analysis were visualized using the ggplot2 R package (<https://cran.r-project.org/web/packages/ggplot2/index.html>).

Western blotting (WB)

Fresh surgical brain tissues were lysed in 1× lysis buffer containing 50 mM Tris pH 6.8, 2% SDS, 0.025% bromophenol blue, 10% glycerol, and 5% BME. Proteins were resolved by 7.5–10% sodium dodecylsulfate–polyacrylamide gel electrophoresis (SDS–PAGE) and transferred to the PVDF membrane. Membranes were blocked with 5% BSA/TBST or skim milk, and incubated with different primary antibodies at 4 °C overnight (application information listed in Supplementary Data 13). Then, washed (by TBST for 3 × 5 min) membranes were probed using HRP-conjugated secondary antibodies. Finally, membranes were developed using ECL substrates (Cat: 180-5001, Tanon) on equipment of Tanon 5200 Chemiluminescence Image Analysis System (Tanon, Shanghai). If required, ImageJ software was used to facilitate the quantification of protein bands.

Immunofluorescence (IF) staining

Fresh surgical brain tissues were washed with PBS three times, followed by fixing in the 4% polyformaldehyde. Before cryosectioning into 30 μm sections, brain tissues were dehydrated in a 30% sucrose solution. IF staining was performed following a standard protocol⁵⁸. The sections were incubated with 0.05% Triton X-100 for 30 min and then sealed with donkey serum blocking solution for 1 hour at room temperature. After removing the blocking solution, sections were incubated with primary antibodies overnight at 4 °C. The next day, sections were washed with TBS 3 × 5 min, and incubated with secondary antibodies at room temperature for 2 h. Finally, the sections were counterstained with DAPI before being sealed in the fluorescence sealing medium. If required, ImageJ software was used to facilitate the quantification of the fluorescence signal. The detailed information on primary antibodies used in this study including FOXP1, FOXP2, SATB2, CUX1, COUP-TF1, NEUN, SP8, CR, PV, SOM, SOX6, VIM, GFAP, etc was listed in Supplementary Data 13.

HE staining

Regarding histology, the excised tissues were preserved in 10% buffered formalin, subsequently embedded in paraffin, and then sliced into 5 μm-thick sections for hematoxylin and eosin staining.

Zebrafish PTZ-seizure model and behavioral analysis

The experiment was approved by the Ethical Committee of the Children's Hospital of Fudan University (IRB 2021-77). Larvae were exposed to either the control group or the Semaxinib group (0.2 μM, a VEGFR inhibitor that induces vascular hypoplasia) from 1 to 5 days post-fertilization (dpf). At 5 dpf, antiseizure efficacy testing was performed⁵⁹. For the experiment, 1.5 mL of 1× EM medium, in which the larvae were housed, was added to 12-well plates. Twelve larvae were placed at the center of each well. In the drug-treated group, larvae were exposed to 3 mM PTZ for 10 minutes, while the control group was treated without PTZ. Time-lapse imaging was used to monitor and record larval movements within the wells over 10 min. Each experimental group was tested in triplicate, with 10 wells per trial ($n = 40$).

Statistics & reproducibility

All experiments subjected to statistical tests were repeated at least three times, of which the detailed replications were specified in the related figure legends. Data were randomly collected, without exclusion. Statistical analyses were performed on GraphPad Prism9 (Boston, USA). Unpaired Student's *t*-test was employed for two-group comparison unless otherwise indicated. $P\text{-value} < 0.05$ was considered as statistically significant.

Reporting summary

Further information on research design is available in the Nature Portfolio Reporting Summary linked to this article.

Data availability

The raw snRNA-seq data generated in this study have been deposited in the database of Genome Sequence Archive for human maintained by China National Center for Bioinformatics under accession code [HRA010445](https://www.genome.gov.cn/hra/HRA010445). Source data are provided with this paper.

References

- Guerrini, R. & Barba, C. Focal cortical dysplasia: an update on diagnosis and treatment. *Expert Rev. Neurother.* **21**, 1213–1224 (2021).
- Lee, H. M. et al. Multimodal mapping of regional brain vulnerability to focal cortical dysplasia. *Brain* **146**, 3404–3415 (2023).
- Kapar, O. et al. Focal cortical dysplasia pathology: diagnostic difficulty, classification, and utility for pathogenesis. *Neurosurg. Focus* **53**, E6 (2022).

4. Pinheiro, J. & Honavar, M. Focal cortical dysplasia: Updates. *Indian J. Pathol. Microbiol.* **65**, S189–s197 (2022).
5. Urbach, H., Kellner, E., Kremers, N., Blumcke, I. & Demerath, T. MRI of focal cortical dysplasia. *Neuroradiology* **64**, 443–452 (2022).
6. Hauptman, J. S. & Mathern, G. W. Surgical treatment of epilepsy associated with cortical dysplasia: 2012 update. *Epilepsia* **53**, 98–104 (2012).
7. Galvão, I. C. et al. Identifying cellular markers of focal cortical dysplasia type II with cell-type deconvolution and single-cell signatures. *Sci. Rep.* **13**, 13321 (2023).
8. Najm, I. et al. The ILAE consensus classification of focal cortical dysplasia: An update proposed by an ad hoc task force of the ILAE diagnostic methods commission. *Epilepsia* **63**, 1899–1919 (2022).
9. Blumcke, I. et al. Neocortical development and epilepsy: insights from focal cortical dysplasia and brain tumours. *Lancet Neurol.* **20**, 943–955 (2021).
10. Iffland, P. H. 2nd, Carson, V., Bordey, A. & Crino, P. B. GATORopathies: The role of amino acid regulatory gene mutations in epilepsy and cortical malformations. *Epilepsia* **60**, 2163–2173 (2019).
11. Lim, L., Mi, D., Llorca, A. & Marin, O. Development and Functional Diversification of Cortical Interneurons. *Neuron* **100**, 294–313 (2018).
12. D’Gama, A. M. et al. Somatic Mutations Activating the mTOR Pathway in Dorsal Telencephalic Progenitors Cause a Continuum of Cortical Dysplasias. *Cell Rep.* **21**, 3754–3766 (2017).
13. Ma, T. et al. Subcortical origins of human and monkey neocortical interneurons. *Nat. Neurosci.* **16**, 1588–1597 (2013).
14. Tahta, A. & Turgut, M. Focal cortical dysplasia: etiology, epileptogenesis, classification, clinical presentation, imaging, and management. *Childs Nerv. Syst.* **36**, 2939–2947 (2020).
15. Xu, Y. & Fan, Q. Relationship between chronic hypoxia and seizure susceptibility. *CNS Neurosci. Ther.* **28**, 1689–1705 (2022).
16. Khoshkhou, S., Lal, D. & Walsh, C. A. Application of single cell genomics to focal epilepsies: A call to action. *Brain Pathol.* **31**, e12958 (2021).
17. Nagy, C. et al. Single-nucleus transcriptomics of the prefrontal cortex in major depressive disorder implicates oligodendrocyte precursor cells and excitatory neurons. *Nat. Neurosci.* **23**, 771–781 (2020).
18. Caglayan, E., Liu, Y. & Konopka, G. Neuronal ambient RNA contamination causes misinterpreted and masked cell types in brain single-nuclei datasets. *Neuron* **110**, 4043–4056.e4045 (2022).
19. Sun, L. et al. Deciphering the temporal transcriptional landscape of human fetal leptomeninges. *Brain* **awae397** <https://doi.org/10.1093/brain/awae397> (2024). Online ahead of print.
20. Tran, M. N. et al. Single-nucleus transcriptome analysis reveals cell-type-specific molecular signatures across reward circuitry in the human brain. *Neuron* **109**, 3088–3103.e3085 (2021).
21. Ma, S. et al. Molecular and cellular evolution of the primate dorsolateral prefrontal cortex. *Science* **377**, eabo7257 (2022).
22. Yang, A. C. et al. A human brain vascular atlas reveals diverse mediators of Alzheimer’s risk. *Nature* **603**, 885–892 (2022).
23. Fu, R. et al. clustifyr: an R package for automated single-cell RNA sequencing cluster classification. *F1000Res* **9**, 223 (2020).
24. von Bartheld, C. S., Bahnay, J. & Herculano-Houzel, S. The search for true numbers of neurons and glial cells in the human brain: A review of 150 years of cell counting. *J. Comp. Neurol.* **524**, 3865–3895 (2016).
25. Mathys, H. et al. Single-cell atlas reveals correlates of high cognitive function, dementia, and resilience to Alzheimer’s disease pathology. *Cell* **186**, 4365–4385.e4327 (2023).
26. Squair, J. W., Skinnider, M. A., Gautier, M., Foster, L. J. & Courtine, G. Prioritization of cell types responsive to biological perturbations in single-cell data with Augur. *Nat. Protoc.* **16**, 3836–3873 (2021).
27. Crowell, H. L. et al. muscat detects subpopulation-specific state transitions from multi-sample multi-condition single-cell transcriptomics data. *Nat. Commun.* **11**, 6077 (2020).
28. Perucca, P., Bahlo, M. & Berkovic, S. F. The Genetics of Epilepsy. *Annu Rev. Genomics Hum. Genet.* **21**, 205–230 (2020).
29. Karatzas, E. et al. Darling: A Web Application for Detecting Disease-Related Biomedical Entity Associations with Literature Mining. *Bio-molecules* **12**, 520 (2022).
30. Le, D. H. & Dao, L. T. M. Annotating Diseases Using Human Phenotype Ontology Improves Prediction of Disease-Associated Long Non-coding RNAs. *J. Mol. Biol.* **430**, 2219–2230 (2018).
31. Newman, A. M. et al. Determining cell type abundance and expression from bulk tissues with digital cytometry. *Nat. Biotechnol.* **37**, 773–782 (2019).
32. Hunt, G. J., Freytag, S., Bahlo, M. & Gagnon-Bartsch, J. A. dtangle: accurate and robust cell type deconvolution. *Bioinformatics* **35**, 2093–2099 (2019).
33. Wu, D. et al. The blood-brain barrier: structure, regulation, and drug delivery. *Signal Transduct. Target Ther.* **8**, 217 (2023).
34. Mishra, A. et al. Astrocytes mediate neurovascular signaling to capillary pericytes but not to arterioles. *Nat. Neurosci.* **19**, 1619–1627 (2016).
35. Poittevin, M. et al. Smooth muscle cell phenotypic switching in stroke. *Transl. Stroke Res.* **5**, 377–384 (2014).
36. Khakh, B. S. & Deneen, B. The Emerging Nature of Astrocyte Diversity. *Annu Rev. Neurosci.* **42**, 187–207 (2019).
37. Orlova, K. A. et al. Early progenitor cell marker expression distinguishes type II from type I focal cortical dysplasias. *J. Neuropathol. Exp. Neurol.* **69**, 850–863 (2010).
38. Iffland, P. H. 2nd & Crino, P. B. Focal Cortical Dysplasia: Gene Mutations, Cell Signaling, and Therapeutic Implications. *Annu Rev. Pathol.* **12**, 547–571 (2017).
39. Crucke, J. & Huysseune, A. Blocking VEGF signaling delays development of replacement teeth in zebrafish. *J. Dent. Res.* **94**, 157–165 (2015).
40. Chung, C. et al. Comprehensive multi-omic profiling of somatic mutations in malformations of cortical development. *Nat. Genet.* **55**, 209–220 (2023).
41. Hester, M. S. et al. Impact of rapamycin on status epilepticus induced hippocampal pathology and weight gain. *Exp. Neurol.* **280**, 1–12 (2016).
42. Kato, M. et al. Sirolimus for epileptic seizures associated with focal cortical dysplasia type II. *Ann. Clin. Transl. Neurol.* **9**, 181–192 (2022).
43. Kadam, S. D. & Dudek, F. E. Temporal progression of evoked field potentials in neocortical slices after unilateral hypoxia-ischemia in perinatal rats: Correlation with cortical epileptogenesis. *Neuroscience* **316**, 232–248 (2016).
44. Josephson, C. B., Rosenow, F. & Al-Shahi Salman, R. Intracranial Vascular Malformations and Epilepsy. *Semin Neurol.* **35**, 223–234 (2015).
45. Goyal, A., Fernandes-Torres, J., Flemming, K. D., Williams, L. N. & Daniels, D. J. Clinical presentation, natural history, and outcomes for infantile intracranial cavernous malformations: case series and systematic review of the literature. *Childs Nerv. Syst.* **39**, 1545–1554 (2023).
46. El Meskine, T., Li, J., Reise, J. & Toffa, D. H. Epilepsy and cerebral developmental venous anomalies (DVAs): A systematic review. *Epileptic Disord.* **25**, 209–217 (2023).
47. Hildebrandt, M. et al. White matter angiopathy is common in pediatric patients with intractable focal epilepsies. *Epilepsia* **49**, 804–815 (2008).
48. Shen, K. F. et al. Vascular endothelial growth factor-C modulates cortical NMDA receptor activity in cortical lesions of young patients and rat model with focal cortical dysplasia. *Brain Pathol.* **32**, e13065 (2022).

49. Zhang, L. et al. Filamin A inhibition reduces seizure activity in a mouse model of focal cortical malformations. *Sci. Transl. Med.* **12**, eaay0289 (2020).
50. Ribierre, T. et al. Targeting pathological cells with senolytic drugs reduces seizures in neurodevelopmental mTOR-related epilepsy. *Nat. Neurosci.* **27**, 1125–1136 (2024).
51. Chun, Y. & Kim, J. AMPK-mTOR Signaling and Cellular Adaptations in Hypoxia. *Int. J. Mol. Sci.* **22**, 9765 (2021).
52. Fleming, S. J. et al. Unsupervised removal of systematic background noise from droplet-based single-cell experiments using CellBender. *Nat. Methods* **20**, 1323–1335 (2023).
53. Yang, S. et al. Decontamination of ambient RNA in single-cell RNA-seq with DecontX. *Genome Biol.* **21**, 57 (2020).
54. Young, M.D. & Behjati, S. SoupX removes ambient RNA contamination from droplet-based single-cell RNA sequencing data. *Gigascience* **9**, giaa151 (2020).
55. Korsunsky, I. et al. Fast, sensitive and accurate integration of single-cell data with Harmony. *Nat. Methods* **16**, 1289–1296 (2019).
56. Velmeshev, D. et al. Single-cell genomics identifies cell type-specific molecular changes in autism. *Science* **364**, 685–689 (2019).
57. Pfisterer, U. et al. Identification of epilepsy-associated neuronal subtypes and gene expression underlying epileptogenesis. *Nat. Commun.* **11**, 5038 (2020).
58. Im, K., Mareninov, S., Diaz, M. F. P. & Yong, W. H. An Introduction to Performing Immunofluorescence Staining. *Methods Mol. Biol.* **1897**, 299–311 (2019).
59. Turrini, L. et al. Optical mapping of neuronal activity during seizures in zebrafish. *Sci. Rep.* **7**, 3025 (2017).

Acknowledgements

We thank the families who donated the tissue samples used in this study. Dashi-Qi was supported by NSFC grants 82271197, 81974175 and Shanghai Natural Science Foundation grant 20ZR1408600. Xinyu-Mei was supported by NSFC grant 82171288, Shanghai Natural Science Foundation grants 22ZR1458100 and Shanghai Municipal Health Commission Youth Science Foundation 20214Y0238. Brain elements (in Figs. 1a and 5h) were created using resources from Scidraw.io, with a brief modification in element color. We acknowledge the Medical Innovation Research Project, Shanghai Science and Technology Innovation Plan of Action grant to Ruizhao (22Y11904400), and NSFC grant to Fayongzhang (81271296).

Author contributions

D.S.-Q. conceived/designed and interpreted the experiments and, with D.S.-Q., X.D.-Z., L.C.-S., Y.J.-L., Y.L., L.Y., J.J.-G, M.W., Y.F.-T., and G.P.-L. conducted the experiments. R.Z., J.S.-Z., and M.W., assisted with

specimen collection. R.Z., M.W., J.S.-Z., X.G. and Y.F.-Z. conducted clinical and neuropathological reviews. C.T.-F., and D.S.-Q. designed and performed the bioinformatic analyses. C.T.-F. and D.S.-Q prepared the figures. D.S.-Q., C.T.-F., and L.Y. wrote the manuscript with input from all authors. D.S.-Q., X.Y.-M., L.Z., M.Z.-R., J.B.-X., and S.J.-M. revised the manuscript.

Competing interests

The authors declare no competing interests.

Additional information

Supplementary information The online version contains supplementary material available at <https://doi.org/10.1038/s41467-025-58535-6>.

Correspondence and requests for materials should be addressed to Rui Zhao, Xinyu Mei or Dashi Qi.

Peer review information *Nature Communications* thanks Ingmar Blumcke, Khodosevich and the other, anonymous, reviewer(s) for their contribution to the peer review of this work. A peer review file is available.

Reprints and permissions information is available at <http://www.nature.com/reprints>

Publisher's note Springer Nature remains neutral with regard to jurisdictional claims in published maps and institutional affiliations.

Open Access This article is licensed under a Creative Commons Attribution-NonCommercial-NoDerivatives 4.0 International License, which permits any non-commercial use, sharing, distribution and reproduction in any medium or format, as long as you give appropriate credit to the original author(s) and the source, provide a link to the Creative Commons licence, and indicate if you modified the licensed material. You do not have permission under this licence to share adapted material derived from this article or parts of it. The images or other third party material in this article are included in the article's Creative Commons licence, unless indicated otherwise in a credit line to the material. If material is not included in the article's Creative Commons licence and your intended use is not permitted by statutory regulation or exceeds the permitted use, you will need to obtain permission directly from the copyright holder. To view a copy of this licence, visit <http://creativecommons.org/licenses/by-nc-nd/4.0/>.

© The Author(s) 2025